



## Original Article

### Lithological mapping using remote sensing techniques: A case study of Alagbayan area, Dornogobi province, Mongolia

Badrakh Munkhsuren<sup>1\*</sup>, Batkhuyag Enkhdalai<sup>1</sup>, Tserendash Narantsetseg<sup>1</sup>, Khurelchuluun Udaanjargal<sup>2</sup>, Demberel Orolmaa<sup>1</sup>, Dolgorjav Munkhjin<sup>1</sup>

<sup>1</sup>Department of Regional Geology and Tectonics, Institute of Geology, Mongolian Academy of Sciences, Ulaanbaatar 15160, Mongolia

<sup>2</sup>Ereenchuluu LLC, Ulaanbaatar 15160, Mongolia

\*Corresponding author: [munkhsuren.b@mas.ac.mn](mailto:munkhsuren.b@mas.ac.mn), ORCID: [0000-0001-8328-128X](https://orcid.org/0000-0001-8328-128X)

## ARTICLE INFO

### Article history:

Received 10 September, 2021

Accepted 26 December, 2021

## ABSTRACT

This study investigated the multispectral remote sensing techniques including ASTER, Landsat 8 OLI, and Sentinel 2A data in order to distinguish different lithological units in the Alagbayan area of Dornogobi province, Mongolia. Therefore, Principal component analysis (PCA), Band ratio (BR), and Support Vector Machine (SVM), which are widely used image enhancement methods, have been applied to the satellite images for lithological mapping. The result of supervised classification shows that Landsat data gives a better classification with an overall accuracy of 93.43% and a kappa coefficient of 0.92 when the former geologic map and thin section analysis were chosen as a reference for training samples. Moreover, band ratios of ((band 7 + band 9)/band 8) obtained from ASTER corresponds well with carbonate rocks. According to PCs, PC4, PC3 and PC2 in the RGB of Landsat, PC3, PC2, PC6 for ASTER data are chosen as a good indicator for different lithological units where Silurian, Carboniferous, Jurassic, and Cretaceous formations are easily distinguished. In terms of Landsat images, the most efficient BR was a ratio where BRs of 5/4 for alluvium, 4/7 for schist and 7/6 to discriminate granite. In addition, as a result of BR as well as PCA, Precambrian Khutag-Uul metamorphic complex and Norovzeeg formation can be identified but granite-gneiss and schist have not given satisfactory results.

**Keywords:** ASTER, Sentinel, Landsat, Support vector machine, Band Ratio

## INTRODUCTION

In recent years, multispectral remote sensing data has been widely used in geological research such as lithological mapping, mineral alteration mapping as well as structural geology (Kumar et al., 2015; Pour et al., 2019; Adiri et al.; 2016; Bentahar et al., 2020). For geological science, the approach of this technique is based on the characteristics of the physical and chemical properties of the different types of rocks. In

detail, these rocks reflect the electromagnetic energy in three areas including visible (400-700 nm), near-infrared (700-1300 nm), and short wave infrared (1300-2500 nm) (Hauff, 2008), which could allow the identification of the spectral absorption features of the mineral composition of the rock (Bachri et al., 2019). Minerals such as iron, copper, and manganese are easily distinguished in the visible areas while spectral information in the near-infrared is

Table 1. The characteristics of spectral bands of Landsat 8 OLI and ASTER, and Sentinel 2A

Landsat 8 Operational Land Imager (OLI)	Bands	Wavelength, $\mu\text{m}$	Resolution, m	ASTER	Bands	Wavelength, $\mu\text{m}$	Resolution, m	Sentinel 2A	Bands	Central Wavelength, $\mu\text{m}$	Resolution, m		
	1	0.43-0.45	30		1	0.520-0.600	15		1	0.443	60		
	2	0.45-0.51			2	0.630-0.690			2	0.49	10		
	3	0.53-0.59			3N	0.780-0.860			3	0.56	10		
	4	0.64-0.67			3B	0.780-0.860			4	0.665	10		
	5	0.85-0.88			4	1.600-1.700	30		5	0.705	20		
	6	1.57-1.65			5	2.145-2.185			6	0.74	20		
	7	2.11-2.29			6	2.185-2.225			7	0.783	10		
	8	0.50-0.68	15		7	2.235-2.285			8	0.842	20		
	9	1.36-1.38	30		8	2.295-2.365			8A	0.865	60		
					9	2.360-2.430			9	0.945	60		
					10	8.125-8.475	90		10	1.375	20		
					11	8.475-8.825			11	1.61	20		
					12	8.925-9.275			12	2.19	20		
					13	10.25-10.95							
					14	10.95-11.65							

useful for garnet, hydroxide, and carbonate minerals (Hauff, 2008). One of the most important advantages of remote sensing is that it could be an affordable and effective method for lithological mapping especially in arid and inaccessible regions (Zhang and Li., 2014; Masoumi et al., 2017; Ge et al., 2018). Therefore, it can be applied to improve the traditional geological mapping process with satellite data, which can be used at no additional cost.

Unfortunately, only a few studies have been mapped previously using remote sensing techniques within the territory of Mongolia (Stolz 2008; Son et al., 2012; Munkhsuren et al., 2019; Son et al., 2019; Son et al., 2021). Apart from this, the study area is located in the Gobi Desert, which spans through the southern and eastern parts of Mongolia. Therefore, the relatively sparse vegetation canopy and an ample rock exposure of this study area could provide an adequate basis for remote sensing techniques.

The Landsat Operational Land Imager (Landsat OLI 8) multispectral data includes 11 spectral bands with a spatial resolution of 30 m, and a panchromatic band, having a spatial resolution of 15 m and two TIR bands which has a spatial resolution of 100 m (Table 1). Advanced

Spaceborne Thermal Emission and Reflection Radiometer (ASTER) data consists of 14 bands, particularly three VNIR bands with 15 m spatial resolution, six SWIR bands with a 60 m resolution and five TIR which have a 90 m spatial resolution (Table 1). Sentinel 2A data is composed of 13 spectral bands in the VNIR and SWIR bands, including four bands at 10 m, six bands at 20 m and three bands at 60 m spatial resolution (Table 1). These data were downloaded for free from the USGS website (<https://glovis.usgs.gov/>) and Earth data (<https://earthdata.nasa.gov/>).

The objective of this study is to compare the possibility of ASTER, Landsat 8 OLI and, Sentinel 2A multispectral sensors for the lithological mapping in the Alagbayan area of Dornogobi province. In this study, Principal Component Analysis (PCA), Band ratio (BR) and Support vector machine (SVP) methods have been carried out to identify lithological units of the area based on the previous geological map and thin section studies of rock samples.

## GEOLOGICAL SETTINGS

Geologically, Alagbayan area is located in the eastern part of the Gobian Tenger Uul Block (Fig. 1A ) (Tomurtogoo, 2017). According to the

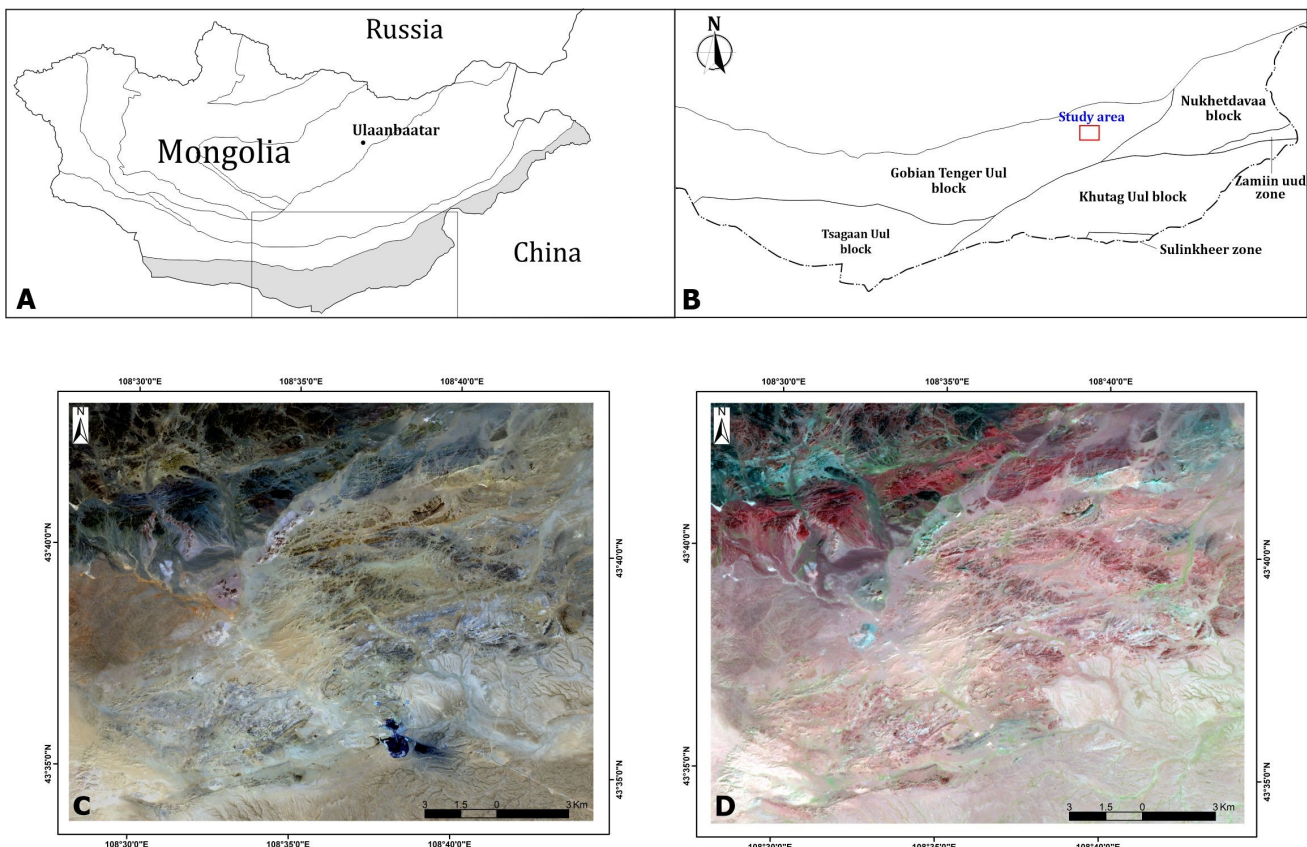


**Fig. 1.** A. Territory of Mongolia; B. Tectonic division of Mongolia showing the study area (Tomurtogoo, 2017); C. Landsat 8 OLI natural color composite image (RGB:432); D. ASTER false-color composite image (RGB:632) of study area which marked in red polygon

State Geological Map of 1:200 000 scale, the area mainly contains metamorphic rocks of Paleoproterozoic and Mesoproterozoic Khutag-Uul metamorphic complex and Norovzeeg formation, which intruded by Neoproterozoic intrusive rocks, and covered by Paleozoic sedimentary and volcanic formations (Fig. 2).

Paleoproterozoic Khutag-Uul (PPhu) metamorphic complex, which is considered to be one of the basement units of the Gobian Tenger Uul block, is widely distributed in the southwestern and central part of the study area. It is about 4-5 km wide and 24 km long extending from Khoshuu Tsav Mountain to somewhat beyond to Ukhna Sair Tolgoi. It dominantly consists of gray, dark gray gneisses, granite-gneisses, brownish-yellow marble limestone, carbonaceous sandstones, and amphibolite (Fig. 2). Moreover, it is intruded by small to medium-grained granite, granodiorite, diorite of the Neoproterozoic Kharangad complex ( $\gamma_2NP_2h$ )

(Fig. 3A) which appears as veins or sills and is unconformably overlain by Baruungoyot formation ( $K_2bg$ ) in the southern part. Khutag-Uul complex is bounded by the fault to the north with Norovzeeg formation ( $MP_{2-3}nz$ ) (Fig. 2) which is dominated by gneiss, granite-gneiss, schist, amphibolite, and calcareous sandstones (Fig. 3C). Khutag-Uul complex and Norovzeeg metamorphic formation, which have not been studied by geochronological research yet and are mainly composed of gneiss, have been classified differently. For instance, according to Bumburuu et al. (2005), the Khutag-Uul and Norovzeeg formations were classified into different formations, but in the 1: 500 000 geological map, they are distinguished by two Paleozoic members.

The Silurian unclassified sedimentary-metamorphic sequence composed of metabasalt, siltstone, siliceous tuff, and sandstone, is extending from Baruun Khukh Ovoo Mountain

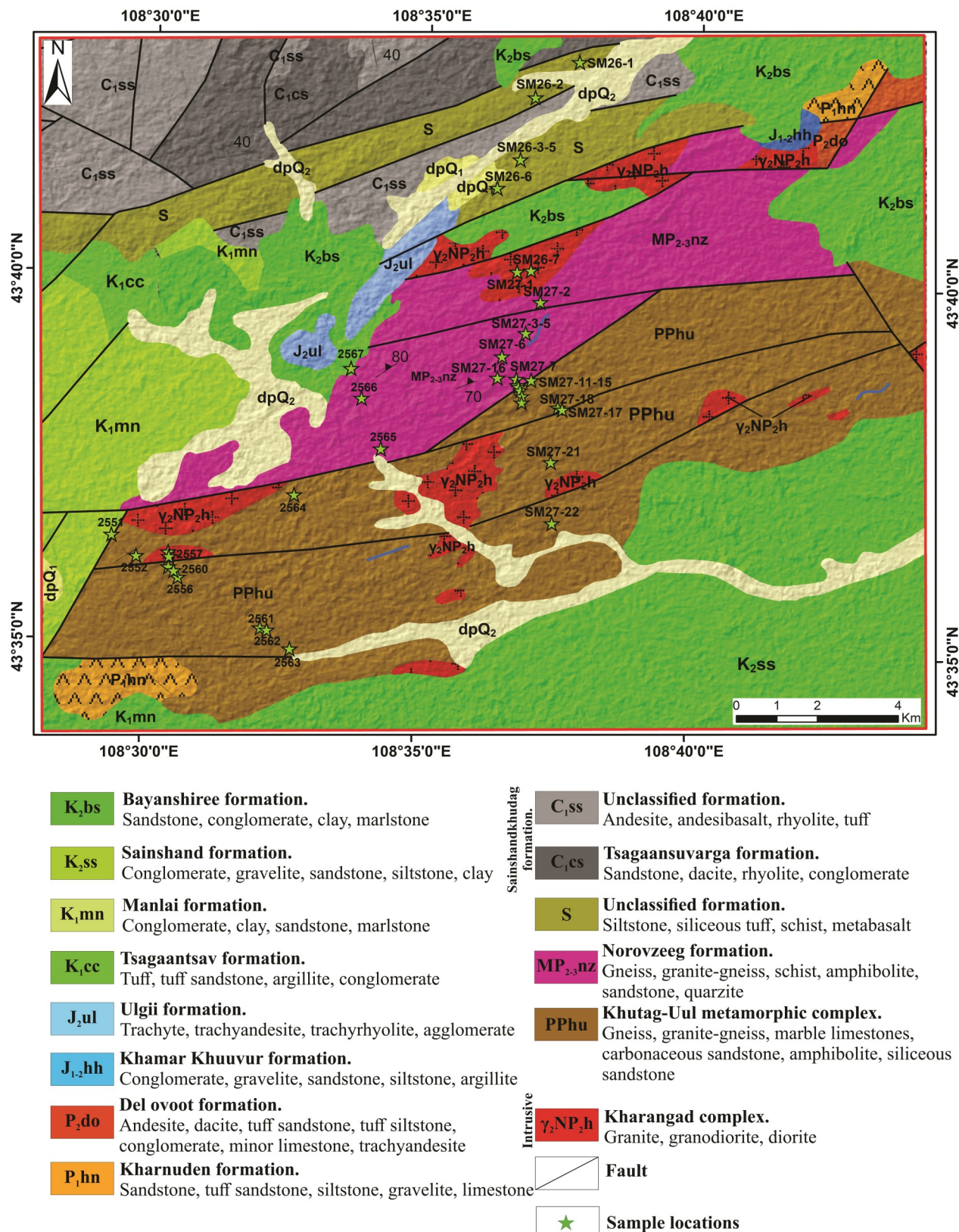


**Fig. 2.** Geologic map of the study area extracted from UGZ 1:200 000 geological mapping project (K49-I) (Bumburuu et al., 2005)

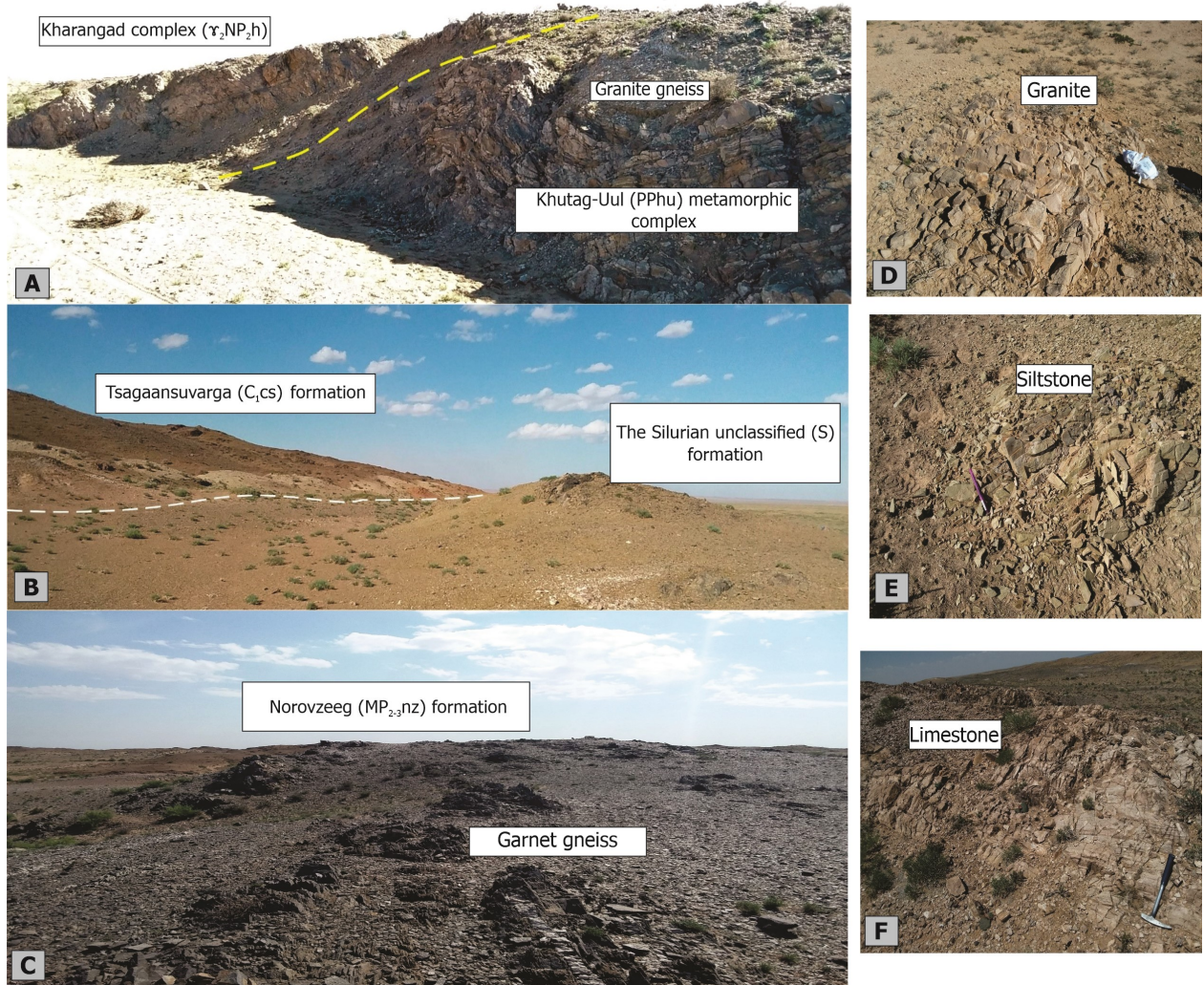


**Fig. 3.** The field photographs of the study area during fieldwork. (A) The contact between granite gneiss from Paleoproterozoic Khutag-Uul metamorphic complex and granite massif from Kharangad complex; (B) The contact between Tsagaansuvarga formation and siltstone of the Silurian unclassified formation; (C) Garnet gneiss of the Norovzeeg formation; (D) Granite sample SM26-7; (E) Siltstone sample SM26-2; (F) Limestone of the Khutag-Uul formation, sample SM27-11

to Khonich Tolgod and is 0.8-1.2 kms wide and 13 km in length. It is adjoined with Sainshandkhudag formation which consists of two members Tsagaansuvarga ( $C_1cs$ ) and unclassified ( $C_{1ss}$ ) formation bounded by the faults (Fig. 2). Tsagaansuvarga ( $C_1cs$ ) formation (Fig. 3B) is spread in a small area and mainly consists of thin layers of dacite, meta-andesite, interbeds of the schist, and sandstone with rhyolite sequence. In the northwestern part of the study area, unclassified Carboniferous ( $C_{1ss}$ ) formation unconformably overlies Tsagaansuvarga formation, which a volcanic

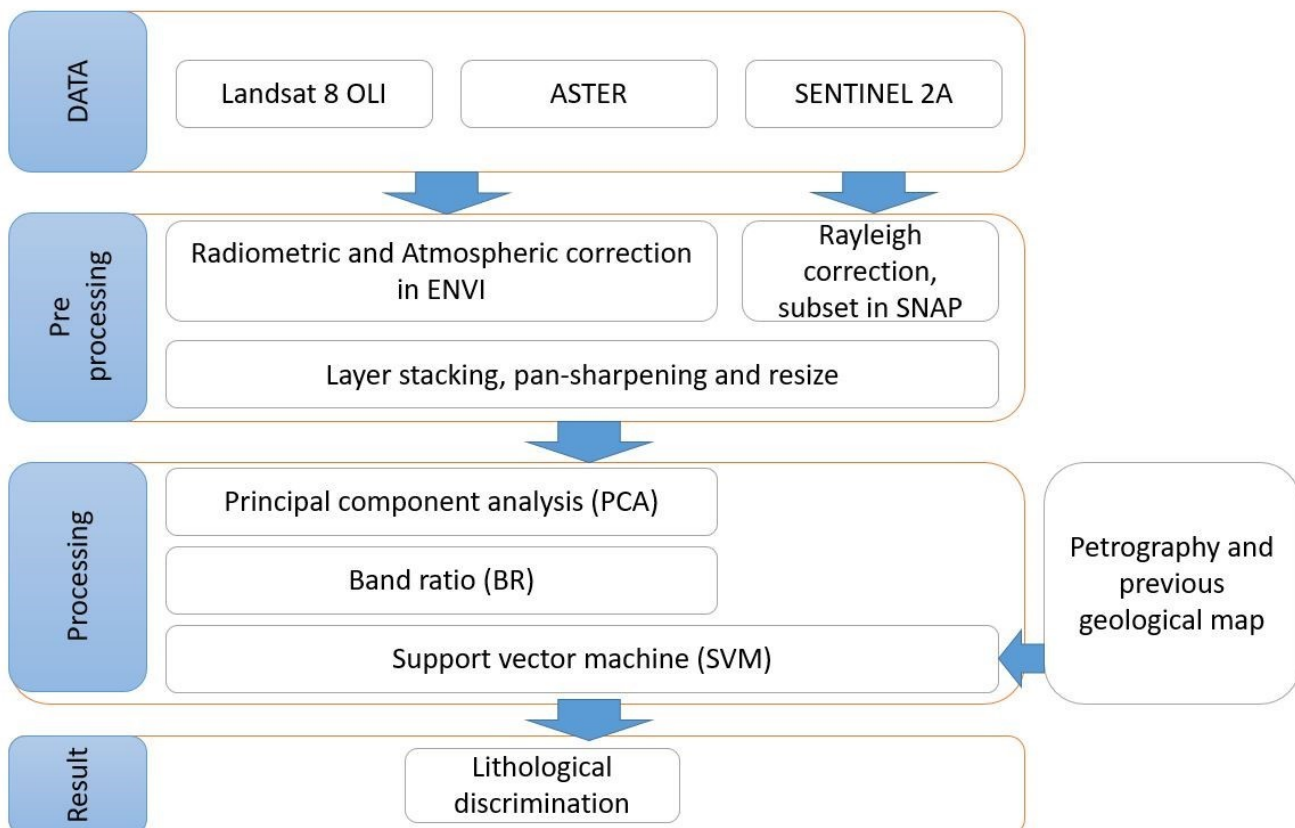
sequence consists mostly of basalt, andesite, and their tuff. Lower and Upper Cretaceous sediments are widely distributed in the study area. They are classified into Manlai ( $K_1mn$ ), Shinehudag ( $K_1sh$ ), Khukhteegeg ( $K_1ht$ ), Sainshand ( $K_2ss$ ), and Baruungoyoot ( $K_2bg$ ) formations. The sediments of these formations usually consist of sandstone, conglomerate, gravel and clay (Fig. 2) (Bumburuu et al., 2005).

## MATERIALS AND METHODS

The fieldwork was carried out during September 2019 and May 2020 to collect rock samples

**Table 2.** Multispectral data used in this study

Data	Acquisition Data	Cloud cover
Landsat OLI 8	4/23/2020	0.0
ASTER L1B	9/21/2002	0.0
Sentinel 2A	9/18/2020	0.0

**Fig. 4.** Flowchart of the methodology

from Silurian unclassified formations, Norovzeeg formation and Khutag-Uul metamorphic complex, Kharangad intrusive complex in this area. We should mention that the former fieldwork was carried out within the framework of the project "The compilation of the State Geological Map at the scale of 1: 200 000 in the K sheet of Mongolia" whereas the latter fieldwork was achieved within the framework of "The basement and cover complexes of the Khatanbulag and South Gobi Massifs: geological development and mineralization" project implemented by the Institute of Geology, Mongolian Academy of Sciences.

The methodology of multispectral data used in

this study is summarized in the flowchart (Fig.4). Three types of cloud-free multispectral data Sentinel-2A, ASTER, and OLI 8 (Table 2) (UTM Zone 49N), as well as thin sections analysis which was conducted with the samples collected from the fieldwork employed in this study. After preprocessing, lithological units were classified using image enhancement and processing methods including Principal Components Analysis (PCA), Band ratio (BR) and Support Vector Machine (SVM) supervised classification technique

**Petrography.** Thirty thin sections of the sedimentary, igneous and metamorphic rocks were investigated using a petrographic

microscope at the Laboratory of Petrography, Institute of Geology, Mongolian Academy of Sciences.

**Preprocessing.** The preprocessing stages included radiometric and atmospheric corrections of the raw data and followed by the Gram-Schmidt Pan-sharpening method that sharpens multispectral bands using high spatial resolution data (panchromatic band 8 for OLI; band 3 for ASTER) in order to create bands with a spatial resolution of 15 m. For ASTER and Landsat data, FLAASH (Fast Atmosphere Analysis of Spectral Hypercubes) was performed on the VNIR and SWIR bands using ENVI 5.3 software. Concerning Sentinel 2A data, the radiometric, atmospheric and resampling processes were automatically performed using the Sentinel Application Platform (SNAP) software by ESA (The European Space Agency) (Ge et al., 2018; Bentahar et al., 2020). Then 13 bands of Sentinel were layer stacked to one file and converted into ENVI. After preprocessing, three multispectral images have been resized between latitudes 43°35'N to 43°45'N and longitudes 108°30'E to 108°45'E. The final images of satellite data were imported as GeoTIFF files into the ArcGIS 10.7 software in order to add geological boundaries.

**Principal component analysis (PCA)** is one of the most effective processing methods of multispectral data which is widely used in geological studies and lineaments mapping (Adiri et al., 2016; Amer et al., 2010; Bentahar et al., 2020; Çörtük et al., 2020). It operates the information in the original raw image to a smaller number of bands called principal components (PCs) (Sabins, 1987; Adiri et al., 2016). In other words, A PC transform creates a smaller dataset from multiple bands, and it rotates them so the data variance is maximized (Chuveico., 2016).

**Band ratio (BR)** is a very effective method for increasing the contrast of particular features which could not be distinguished from the original image data (Rowan and Mars, 2003; Çörtük et al., 2020). Therefore, this method is

widely used in lithological and alteration mapping (Rowan and Mars 2003; Adiri et al. 2016, Pour et al., 2019). Generally, it divides a band by another band (in the simplest case) based on the object's spectral signature (Adiri et al., 2016). Based on the spectral characteristics of rocks and minerals, different types of band ratios have been generated for lithological units. To illustrate, Rowan et al. (2003) recommended ASTER band ratio of (band 6 + band 8)/band 7 to identify carbonate rocks based on Ca-CO<sub>3</sub> spectral absorption, Adiri et al. (2016) have studied Landsat 8 OLI band ratios of 6/5, 5/4, 4/7 for clay, alluvium and schist. The majority of the previous studies have used ASTER and Landsat OLI data for the BR technique (Rezaei et al., 2019; Ourhzif et al., 2019; Hamimi et al., 2020, Çörtük et al., 2020). That is the reason why we only used this method on ASTER and Landsat data.

**Support Vector Machine (SVM)**, which was initially invented by Vapnik in 1979, is one of the most widely used supervised classification methods for lithological mapping (Platt, 1998; Adiri et al., 2016; Ge et al., 2018; Bachri et al., 2019). The principle mechanism of SVM is based on a hyperplane that separates two classes including a set of positive examples and a set of negative and maximizes the margin between these two classes (Platt, 1998; Bentahar and Raji., 2020). SVM requires the selection of regions of interest that represent different lithological units in the study area. Region of interests, also called training samples, are defined based on petrography analysis and geological map in this study.

## RESULTS AND DISCUSSION

### Petrography

We classified rock samples into six groups based on their petrographic characteristics as following: 1-Sandstone (unclassified Silurian formation); 2- Metabasalt (unclassified Silurian formation); 3- Limestone; 4-Granite (Kharangad intrusive complex); 5- Garnet-biotite gneiss; 6-Garnet-biotite-muscovite schist (Fig. 5). Petrographic studies were used to apply the SVM algorithm in this study.

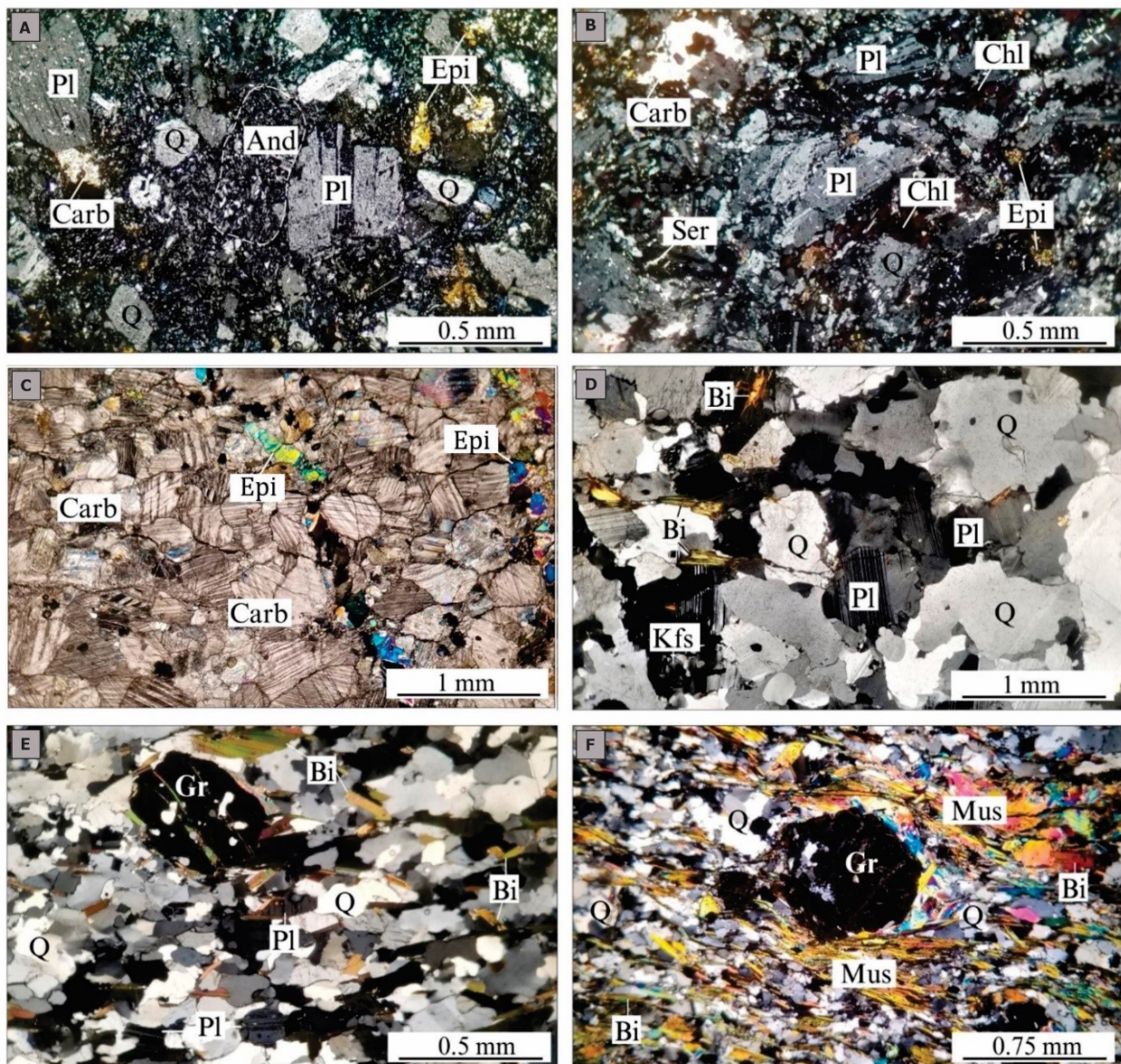


**Fig. 5.** Representative microphotographs of rocks from the Alagbayan area. A) Sandstone (sample SM26-2), B) Metabasalt (sample SM26-6), C) Limestone (sample SM27-11), D) Granite (sample SM26-7), E) Garnet-biotite gneiss (sample SM27-1), F) Garnet-biotite-muscovite schist (sample SM27-4). Abbreviations: Q - quartz, Pl - plagioclase, And - andesite, Carb - carbonite, Epi - epidote, Chl - chlorite, Ser - sericite, Cal - calcite, Kfs - K-feldspar, Bi - biotite, Gr - garnet, Mus - muscovite. All photomicrographs are under cross-polarized light.

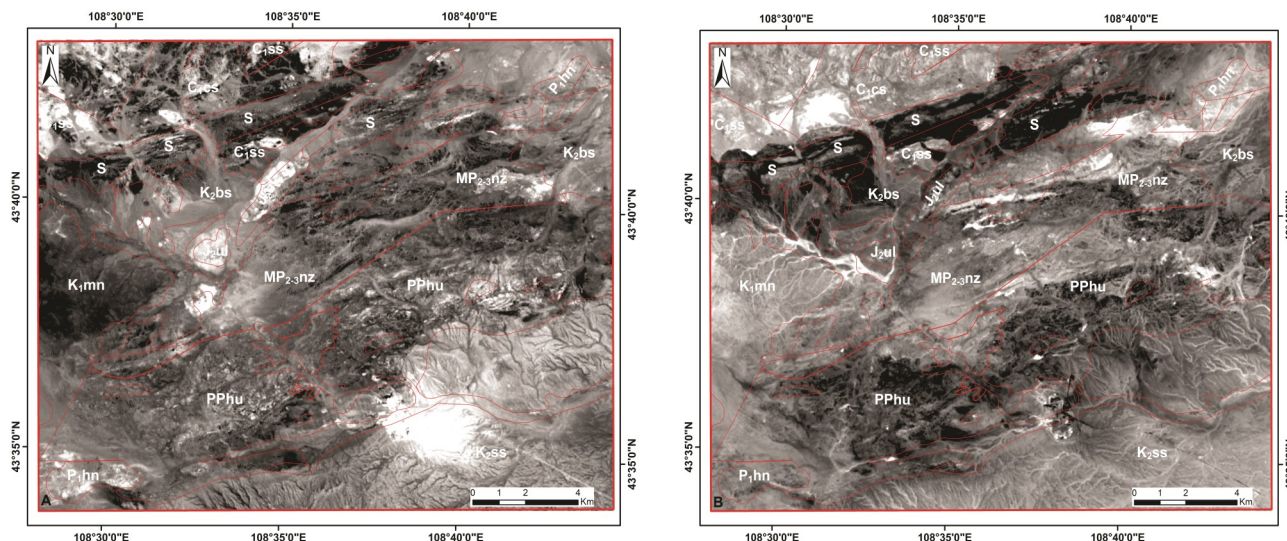
**Medium to coarse-grained sandstone (sample SM26-2)** is made up of framework grains (70-75%), matrix, and cement. Additionally, it comprises sub-angular to angular grains and is generally poorly sorted. The framework grains dominantly include plagioclase, quartz, epidote and in minor sericite carbonate and andesite fragments. Its grain size ranges from 0.1-1.25 mm. The matrix, which constitutes around

between 10 and 15% of the overall composition, is mostly silicate minerals such as quartz and plagioclase (Fig. 5A)

**Metabasalts (sample SM26-06; SM26-05)** are mainly composed of plagioclase (40-45%), chlorite, epidote (25-30%) whereas secondary minerals are sericite (8-10%), quartz (8-10%), carbonate (3-5%) with a minor amount of muscovite aggregates. The rock is

**Table 3.** The characteristics of spectral bands of Landsat 8 OLI and ASTER

PC bands	Band 1	Band 2	Band 3	Band 4	Band 5	Band 6	Band 7
PC1	0.124847	0.148538	0.24966	0.365393	0.459118	0.538837	0.515143
PC2	0.301287	0.313623	0.340048	<b>0.38247</b>	0.363199	-0.39202	-0.51319
PC3	-0.39938	-0.38935	-0.2312	0.106444	<b>0.426884</b>	0.387469	<b>-0.5401</b>
PC4	0.330993	0.256257	0.177331	-0.12521	-0.44134	0.63569	-0.42282
PC5	-0.39235	-0.28259	0.463695	0.565717	-0.47991	-0.02792	0.0075
PC6	0.336421	-0.02427	-0.68949	0.603159	-0.21609	0.007048	0.017012
PC7	0.597877	-0.76281	0.216162	-0.09676	0.057242	-0.03035	0.019653

**Fig. 6.** A) PC2, B) PC3 images of Landsat OLI data

hypidiomorphic in texture and strongly altered which makes it difficult to make clear the original rock (Fig. 5B).

**Limestone (sample SM27-11)** (Fig. 3F). Calcite, epidote, quartz are the minerals presented in thin sections. The minerals are subhedral and anhedral forms. Moreover, the majority of the calcite grains are light brown in color and 0.25-1 mm in size. It displays rhombohedral cleavage and some grains show polysynthetic twinning. The rock is intruded by a 0.2-0.5 wide epidote vein which has a greenish to bluish interference color (Fig. 5C).

**Granite (sample SM26-7)** (Fig. 3D) consists of quartz (60-65%), plagioclase (20-25%), K-feldspar (8-10%), biotite (5-8%) and ore minerals as accessory minerals. The rock is granoblastic in structure and xenomorphic in texture. The grain size of quartz is between 0.25 and 1.5 mm and euhedral form. Plagioclase, as

well as K-feldspar are 0.25-0.75 mm in length while the grain size of biotite ranges from 0.05-0.2 mm (Fig. 5D).

**Garnet-biotite gneiss (sample SM27-1)** is medium to coarse-grained and mainly composed of quartz (60-65%), plagioclase (10-15%), biotite (15-20%) and a trace amount of garnet (5-10%). The grain size of quartz is up to 1.25 mm with serrated margins. Plagioclase shows polysynthetic twinning and grain size ranges from 0.2-0.75 mm. Biotite exhibits brown and subhedral and is about 0.3-1.0 in length. Garnet is euhedral and 0.2-2.2 in size (Fig. 5E).

**Garnet-biotite-muscovite schist (sample SM27-4)** is fine to medium-grained and consists of quartz (50-55%), muscovite (30-35%), garnet (8-10%) with minor amounts of biotite-chlorite (5-10%). The rock is strongly deformed and xenomorphic in texture. Garnet is euhedral and from 0.25 to 1.25 mm in size. The

grain size of aggregates of biotite and chlorite ranges between 0.05-0.1mm (Fig. 5F).

### Principal component analysis (PCA)

To discriminate the different rock units within the study area, the PCA method was applied to the ASTER and Landsat OLI images and results are presented in Fig. 5- Fig. 8. We also used this method on Sentinel satellite imagery, but did not include it in the results section because they did not show good results compared to the other two data.

In this study, a standard transformation of the PCA has been applied by using ENVI 5.3 software utilizing VNIR-SWIR bands of Landsat 8 OLI. In the PCs images, geological formation is mapped by bright pixels if the

eigenvector values are positive in the band. Conversely, if the value is negative, it will be mapped by dark pixels (Çörtük et al., 2020). According to the eigenvectors calculated from Landsat (Table 3), in PC2, Ulgii formation which mainly consists of trachyte and trachyandesite may be distinguished by bright pixels with a positive value (**0.38247**) in band 2 (Fig. 6A). Moreover, PC3 shows a negative high value in band 7 (**-0.5401**) which can be indicated by the Silurian unclassified sedimentary-metamorphic sequence (S) (Fig. 6B). The alluvium is mapped by bright pixels in the same PC with a high positive value of **0.426884** (Fig. 6B). Therefore, the images consist of PC4, PC3, and PC2 in the RGB were chosen as an effective

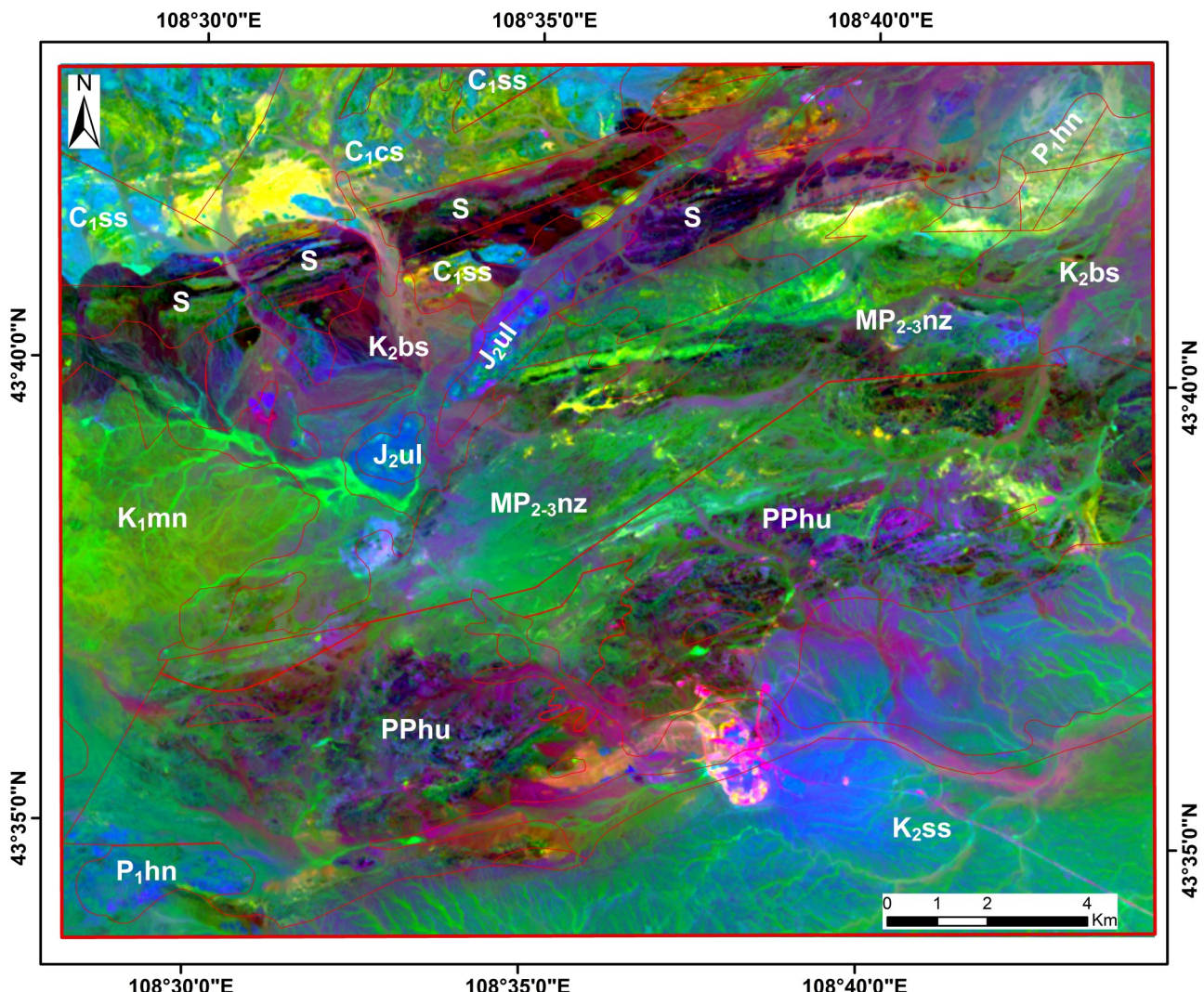
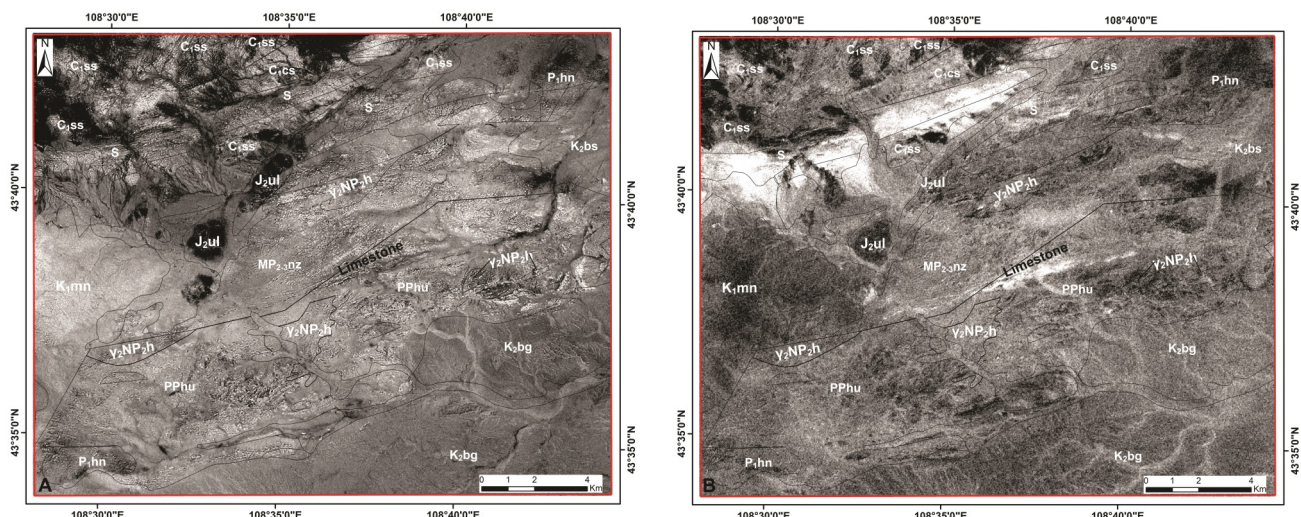


Fig. 7. RGB color composite of PC images Landsat OLI (PC4, PC3, PC2)

**Table 4.** The matrix of eigenvectors for PCA calculated from ASTER data

PC bands	Band 1	Band 2	Band 3	Band 4	Band 5	Band 6	Band 7	Band 8	Band 9
PC1	-0.314864	-0.496449	-0.777038	-0.197449	-0.049495	-0.046237	-0.052029	-0.041133	-0.051377
PC2	-0.686541	-0.467061	0.531409	0.165298	0.00208	0.003418	0.020614	0.016603	0.008937
PC3	-0.040217	0.046403	<u>-0.28939</u>	0.83428	0.254245	0.212331	0.216795	0.15044	0.19262
PC4	0.646266	-0.727192	0.171288	0.075899	0.10273	0.084444	0.006923	-0.019711	0.017642
PC5	0.073909	-0.007804	-0.025829	0.474142	-0.416033	-0.4411	-0.300784	-0.281806	-0.481104
PC6	-0.068415	0.065651	0.003166	-0.007641	<u>0.525784</u>	0.450226	-0.410448	-0.463249	-0.358778
PC7	-0.004198	0.001846	0.007245	-0.074541	0.576499	-0.507204	0.421247	0.142643	-0.454937
PC8	-0.004926	0.002835	-0.000262	0.035696	0.366136	-0.537298	-0.454013	-0.15853	0.587103
PC9	-0.007763	0.007001	0.000954	-0.014411	-0.080086	-0.049168	0.55435	-0.797195	0.219151

**Fig. 8. A) PC3, B) PC6 images of ASTER**

indicator for different lithological units (Fig. 7) where Cretaceous sediments mainly appear as neon green whereas *J<sub>2</sub>ul* formation is shown in blue. Some parts of the Khutag-Uul metamorphic complex are shown in mixed dark purple color while quaternary sediments can be distinguished by their light purple color. It is obvious that this PC band combination is helpful to discriminate Silurian and Jurassic formations where *S* appears dominantly dark tones and *J<sub>2</sub>ul* are indicated by blue color. Two members of Sainshandkhudag formation are distinguished from each other by yellow and light blue tones. Nevertheless, limestone and sedimentary rocks from Kharnuden formation have not been mapped in the PC image of Landsat data (Fig. 7).

Turning to the eigenvectors extracted from the PC images for the ASTER data (Table 4), rocks of *J<sub>2</sub>ul* and *C<sub>1</sub>ss* which are dominantly

composed of trachyte, andesite, trachyandesite (Fig. 2) are mapped by dark pixels where PC3 has an absorption in band 3 with a negative value (-0.28939) (Fig. 8A). PC6, meanwhile, has an absorption in band 5 with a positive contribution (0.525784) where the Silurian formation is mapped in bright pixels (Fig. 8B). It can be seen from the RGB color composite PC image (PC3, PC2, PC6) (Fig. 9) that volcanic rocks from *J<sub>2</sub>ul* and *C<sub>1</sub>ss* formations are shown in green color while Silurian rocks are distinguished as purple color. Khutag-Uul and Norovzeeg formations are predominantly shown in pink color. Additionally, compared to PC images of Landsat data, alluvium sediments are more distinguished in PC images from ASTER, appearing in pale green. Despite their similar lithology, Cretaceous formations are indicated differently. *K<sub>1</sub>mn* formation is mapped in orange tone while *K<sub>2</sub>ss* formation mainly appears as

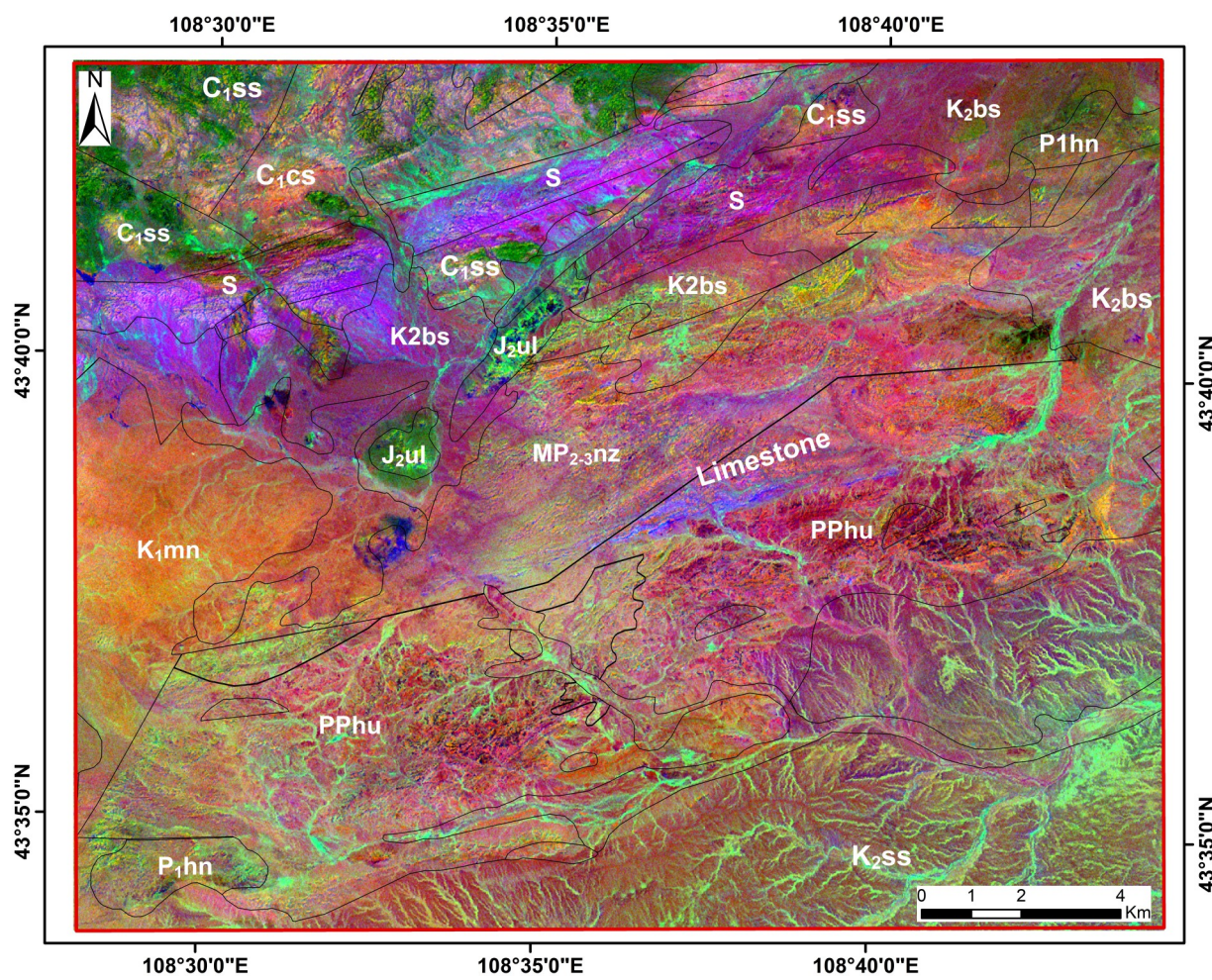


**Fig. 9.** RGB color composite of PC images of ASTER (PC3, PC2, PC6)

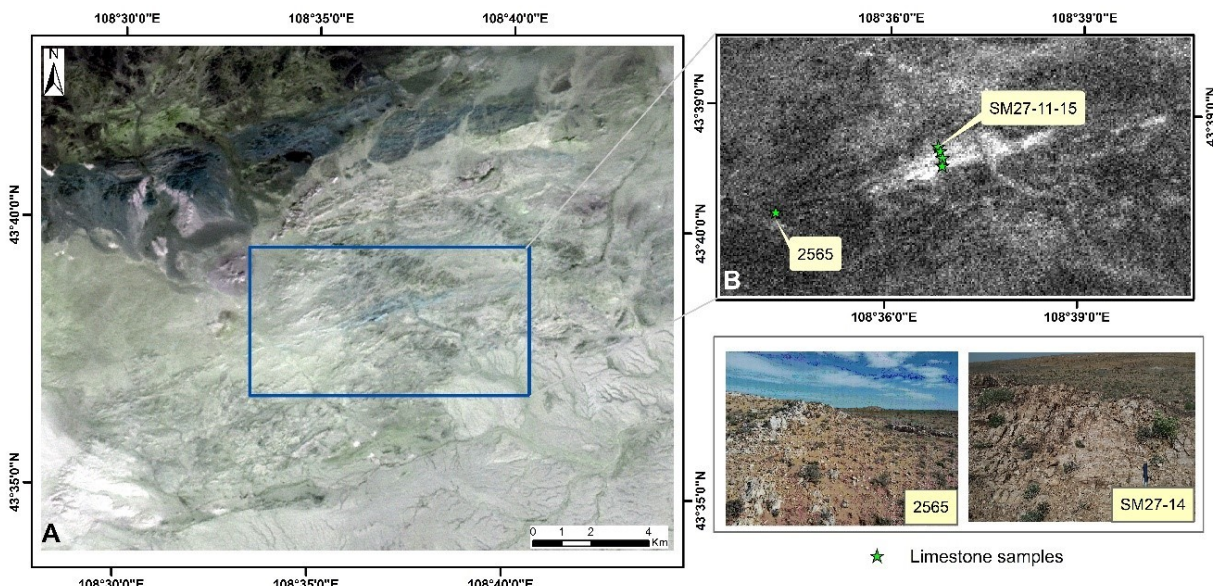


**Fig. 10.** A. ASTER false-color composite image (RGB: 879); B. Grayscale images of ((band 7 + band 9)/band 8) with limestone samples

brown and pink tone. Limestone is distinguished in the ASTER PC image, displaying bluish-purple color (Fig. 9).

### Band ratio (BR)

In this study, we have experienced the different types of band ratios recommended by other studies in order to improve the detection of various lithological units.

Previous studies proposed that multispectral images, especially ASTER, play an important role in the detection of carbonate rocks (Rowan and Mars, 2003; Ninomiya, 2002). To detect the possibility of limestone using ASTER VNIR-SWIR data, we used the band ratio suggested by Rowan and Mars (2003). According to their study, BRs of  $((\text{band 7} + \text{band 9})/\text{band 8})$ ,

representing  $\text{CaCO}_3$  absorption, correspond well with the limestone distribution in lithological mapping. Moreover, those carbonate rocks were mapped in light blue color in the false-color composite image of ASTER where band879 in the RGB (Fig. 10A, B).

We also used BRs (7/6, 6/5, 6/4 as RGB) which were used for distinguishing gneiss and granites (Watts and Harris, 2005; Rezaei et al., 2019). As presented in Fig. 11, BRs (7/6, 6/5, 6/4 as RGB) results show that the metamorphic Khutag-Uul formation, and northeastern part of Norovzeeg formation were differentiated from the adjacent rocks by the purple color. On the other hand, two members of Sainshandkhudag formation, Silurian unclassified formation were highly distinguished with different colors. Granite

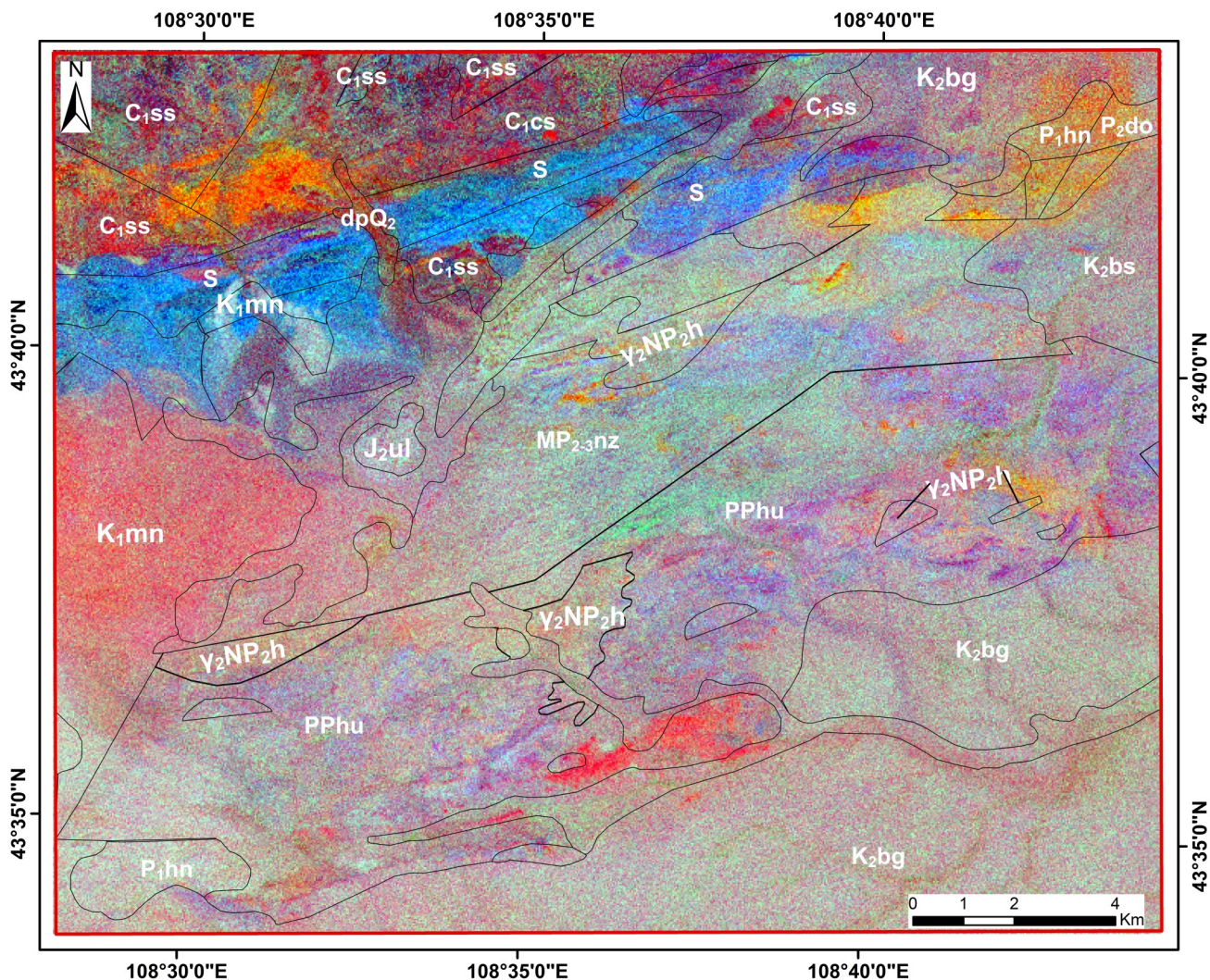


**Fig. 11.** False color composite image of ASTER: BRs (RGB: 7/6, 6/5, 6/4)

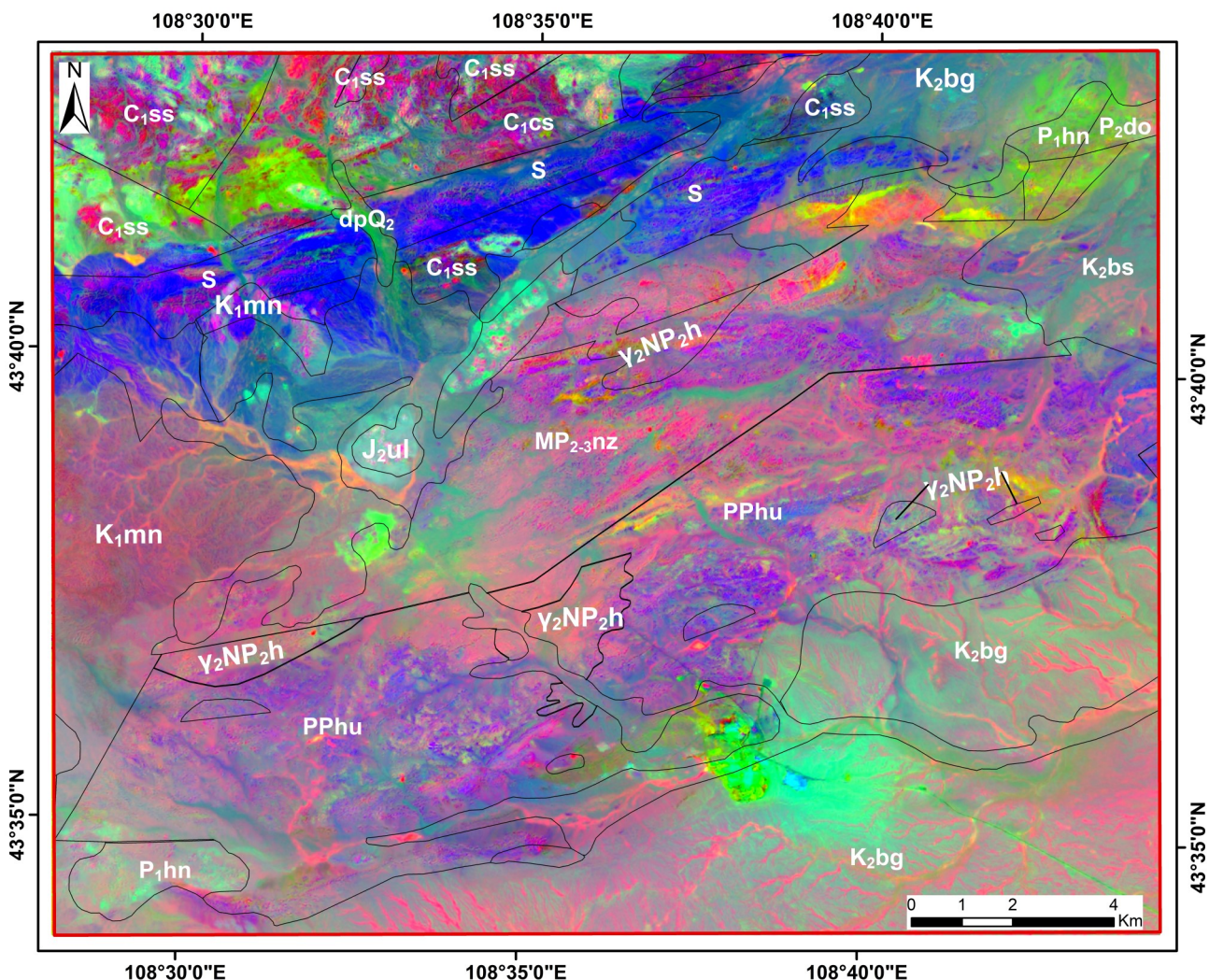


Fig. 12. (5/4, 4/7, 7/6 as RGB) false-color composite of Landsat image

(Kharangad intrusive complex) and gneiss were not clearly distinguished, which may be due to the sparse exposure of the rocks. Previous studies have suggested (Watts and Harris, 2005) that the 7/6 band ratio is related to muscovite absorption, but it is difficult to comment that what kind type of rock is associated with this red area because we have not conducted field works in this part (Fig. 11).

For Landsat data, after examining various band ratios, the most useful BR was a ratio, which Adiri et al. (2016) proposed, where BRs of 5/4 to discriminate alluvium, 4/7 for schist and ratio of 7/6 were used to identify granite with biotite (Fig. 12). Here, Silurian formation is identified by a blue color while alluvium sediments appear pinkish. Compared to PC and SVM of OLI

image, limestone is distinguished in this band ratio. Regarding Khutag-Uul and some parts of Norovzeeg formation, they are mapped by a pinkish color. But similar to other methods, granite and gneiss could not have been distinguished well (Fig. 12).

#### **Support Vector Machine (SVM).**

The output results of classification by SVM of Landsat, ASTER and Sentinel images are shown in Fig. 13. Moreover, Fig. 14 displays overall accuracy for different rock units conducted with three data. In this study, rock samples collected from the field and former geological map shown in Fig. 1 were used as a reference for the region of interests (ROIs). As mentioned earlier, we classified field samples into six categories based

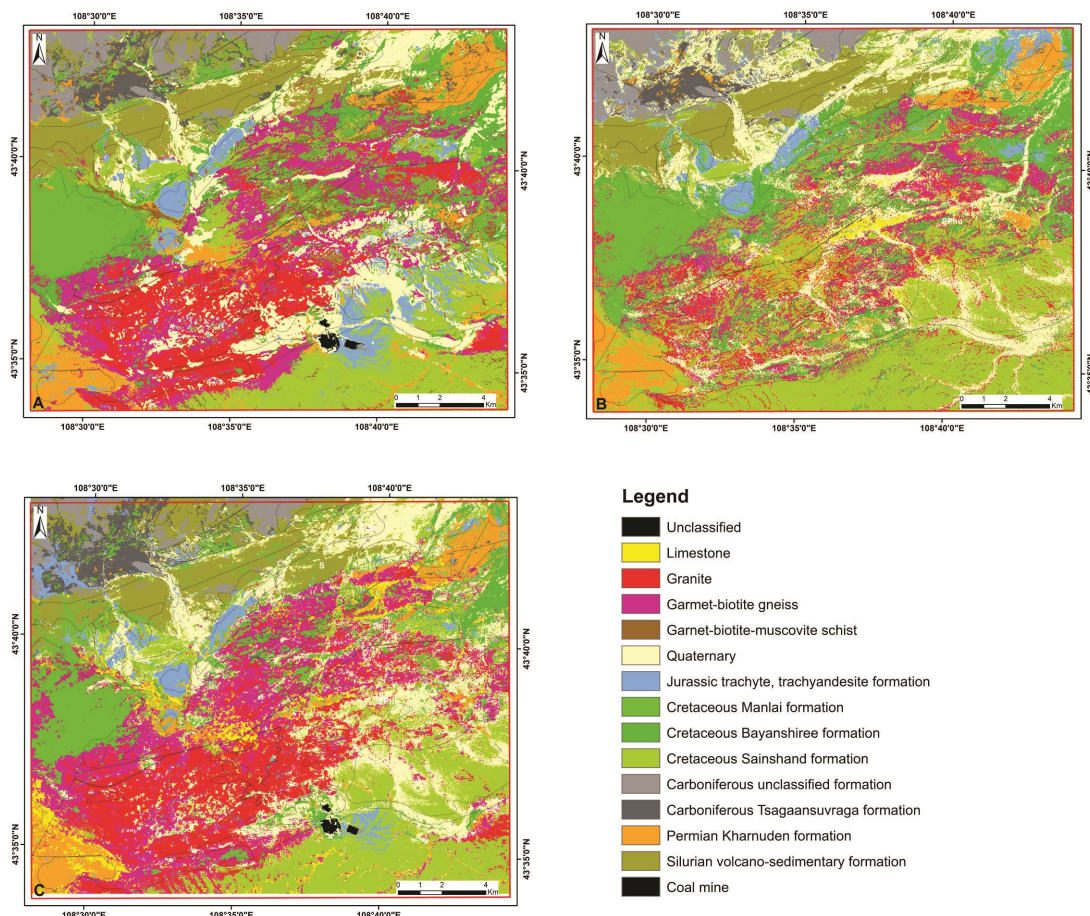


**Fig. 13.** Results of SVM classification A) Landsat OLI; B) ASTER; C) Sentinel 2A

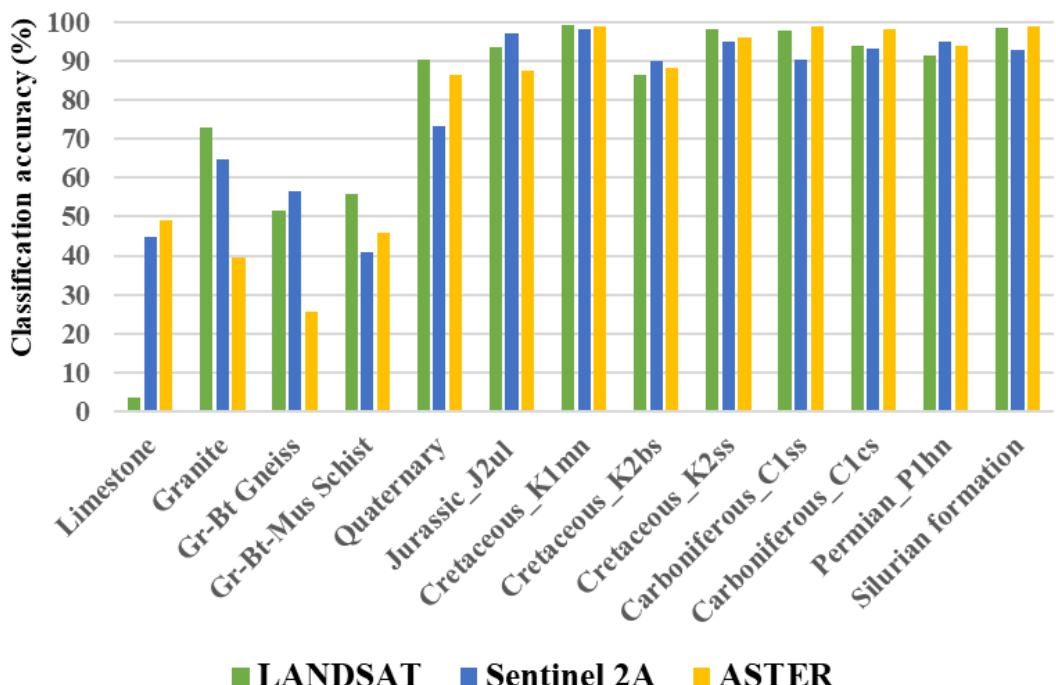


**Fig. 14.** The classification accuracies of the Landsat, ASTER, Sentinel images using the SVM method

on the field observation and petrography analysis (Silurian metabasalt, sandstone, limestone, granite, Gr-Bt gneiss, Gr-Bt-Mus schist). In addition, the remaining lithological units that have not been included in the field study were selected for ROI based on the geological map (Fig. 2) (except Khamar Khuuvur and Del Ovoot formation, due to its small areas). Therefore, a total of 13700 pixels of ROI for the fourteen lithological units were conducted with Landsat OLI, ASTER, Sentinel 2A images. After SVM images, the estimation of the classification accuracy was calculated by the confusion matrix using ROIs for ground truth. It shows what percentage of the ROI pixels were or were not contained in a resulting class (Fig. 14). The overall accuracy of the classification was 93.43% for Landsat OLI, 91.7% for ASTER and 90.3% for Sentinel 2 with kappa coefficients of 0.92, 0.90, and 0.8, respectively. As a result, compared to ASTER and Sentinel, Landsat 8 OLI illustrated a better capability for lithological units, especially in classifying Cretaceous formations, schist and quaternary sediments (Fig. 14). On the other hand, limestone was classified greater in ASTER and corresponded well with the result of band ratio presented in Fig. 10.

However, there were few misclassifications of some lithological units obtained from Sentinel and Landsat images. To illustrate, trachyte and trachyandesite from Jurassic Ulgii formation were mapped southern part of the study area near the coal mine, but it had been mapped previously by the Cretaceous formation in the geological map (Fig. 2 and Fig. 13A, C). Compared to the geological map, it can be seen that intrusive rocks mapped by red in Fig. 13 were widely distributed in Landsat and Sentinel images. But during the fieldwork, there was not much intrusive exposure, thus we believe that this result was incorrectly classified in some areas.

## CONCLUSION

In the present study, the lithological discrimination of the Alagbayan area which is located in Mandakh soum, Dornogobi province, has been achieved using Landsat 8 OLI, ASTER and Sentinel 2A. In detail, Principal component

analysis (PCA), Band ratio (BR) and Support Vector Machine (SVM) have been used based on VNIR and SWIR regions. PCA transformation was carried out with images of ASTER and Landsat whereas Sentinel with these two data was used for SVM supervised classification. Additionally, instead of using spectral signatures extracted from satellite images, this study has been used different band ratios which suggested by other studies (Rowan and Mars, 2003; Watts and Harris, 2005; Rezaei et al., 2019; Adiri et al., 2016). In terms of PC analysis, both chosen PC band combinations of Landsat and ASTER show an excellent correlation with different formations such as Silurian, Carboniferous, Jurassic, and Cretaceous formations. Moreover, compared to PC images of Landsat data, alluvium sediments and limestone are more classified in PC images from ASTER, appearing in pale green and pinkish color. Similar to other studies, ASTER was a high potential data for carbonate rock in the band ratio technique. When it comes to supervised classification, former geological maps and thin section analysis were used as a reference for training samples. As a result, Landsat showed a better capability with an overall accuracy of 93.43% and a kappa coefficient of 0.92 but few misclassifications have been presented, especially for Landsat and Sentinel data. At the beginning of the study, one of the main goals was to identify the oldest metamorphic strata which are Khutag-Uul and Norovzeeg, by remote sensing techniques. But the study showed that most parts of Khutag-Uul complex and the southeastern part of Norovzeeg formation were generally mapped by the same tone in BR and PC analysis. On the other hand, granites and gneisses which are widely distributed in the above two formations could not be distinguished.

In conclusion, lithological classification is an important application to facilitate geological mapping which takes a long time, high-costly process. In our future study, we are planning to use other image processing methods (e.g. Minimum Noise Fraction (MNF) and other Supervised classification techniques) to improve lithological discrimination.

## ACKNOWLEDGEMENTS

The authors would like to express their sincere thanks to anonymous reviewers for their helpful comments and recommendations. This work is part of the project named “The basement and cover complexes of the Khatanbulag and South Gobi Massifs: geological development and mineralization” implemented at the Institute of Geology, Mongolian Academy of Sciences.

## REFERENCES

- Adiri, Z., El Harti, A., Jellouli, A., Maacha, L., Bachaoui, E.M. 2016. Lithological mapping using Landsat 8 OLI and Terra ASTER multispectral data in the Bas Drâa inlier, Moroccan Anti Atlas: Journal of Applied Remote Sensing, v. 10(1), 016005.  
<https://doi.org/10.1117/1.JRS.10.016005>
- Amer, R., Kusky, T., Ghulam, A. 2010. Lithological mapping in the central Eastern Desert of Egypt using ASTER data: Journal of African Earth Sciences, v. 56(2), p. 75-82.  
<https://doi.org/10.1016/j.jafrearsci.2009.06.004>
- Bachri, I., Hakdaoui, M., Raji, M., Teodoro, A.C., Benbouziane, A. 2019. Machine learning algorithms for automatic lithological mapping using remote sensing data: A case study from Souk Arbaa Sahel, Sidi Ifni Inlier, Western Anti-Atlas, Morocco: ISPRS International Journal of Geo-Information, v. 8 (6), p. 1-20.  
<https://doi.org/10.3390/ijgi8060248>
- Bentahar, I., Raji, M. 2020. Comparison of Landsat OLI, ASTER, and Sentinel 2A data in lithological mapping: A Case study of Rich area (Central High Atlas, Morocco): Advances in Space Research. v. 67.  
<https://doi.org/10.1016/j.asr.2020.10.037>
- Bumburuu, G., Boldbaatar, G., Amarjargal, A., Altanshagai, Sh., Ganbaatar, T., Ariunzul, B. 2005. Report of the project of compilation of the 1: 200 000 scale Geological Map of Mongolia. State Geological Fund of Mineral Resources and Petroleum Authority of Mongolia. №K-49-I. (in Mongolian)
- Chuveico, E. 2016. Fundamentals of satellite remote sensing: An environmental approach. 2<sup>nd</sup> edition. CRC Press: Boca Raton, FL. 468 pp. <https://doi.org/10.1177/2399808317711988>
- Çörtük, R.M., Çelik, Ö.F., Alkan, A., Özkan, M., Özyavas, A. 2020. Distribution of rocks in Pinarbas Ophiolite from central Anatolia (Turkey) based on analysis of ASTER and Landsat-8 data: Geological Journal. v.5(10), p. 6810-6822.  
<https://doi.org/10.1002/gj.3844>
- Ge, W., Cheng, Q., Jing, L., Armenakis, C., Ding, H. 2018. Lithological discrimination using ASTER and Sentinel-2A in the Shibanjing ophiolite complex of Beishan orogenic in Inner Mongolia, China: Advances in Space Research. v.62, p. 1702-1716  
<https://doi.org/10.1016/j.asr.2018.06.036>
- Hamimi, Z., Hagag, W., Kamh, S., El-Araby, A. 2020. Application of remote-sensing techniques in geological and structural mapping of Atalla Shear Zone and Environs, Central Eastern Desert, Egypt: Arabian Journal of Geosciences. v. 13(414). p. 1-27.  
<https://doi.org/10.1007/s12517-020-05324-8>
- Hauff, P. 2008. An overview of VIS-NIR-SWIR field spectroscopy as applied precious metals exploration. Arvada, Colorado; Spectral Inc., 80001 303403 8383.
- Kumar, C., Shetty, A., Raval, S., Sharma, R., Ray, P.K.C. 2015. Lithological Discrimination and Mapping using ASTER SWIR Data in the Udaipur area of Rajasthan, India: Procedia Earth and Planetary Sciences, v. 11, p. 180-188.  
<https://doi.org/10.1016/j.proeps.2015.06.022>
- Pour, A.B., Hashim, M., Hong, J.K., Park, Y. 2019. Lithological and alteration mineral mapping in poorly exposed lithologies using Landsat-8 and ASTER satellite data: North-eastern Graham Land, Antarctic Peninsula: Ore Geology Reviews. v. 108, p. 112-133.  
<https://doi.org/10.1016/j.oregeorev.2017.07.018>
- Masoumi, F., Eslamkish, T., Abkar A.A., Honarmand, M., Harris, J.R. 2017. Integration of spectral, thermal, and textural features of ASTER data using Random Forests classification for lithological mapping: Journal of African Earth Sciences, v. 129, p. 445-457.  
<https://doi.org/10.1016/j.jafrearsci.2017.01.028>
- Munkhsuren, B., Odgerel, D., Oyunchimeg, T. 2019. Lithological mapping of Ikh Tsakhir area using remote sensing techniques: Compilation of works of young scientists and researchers in the field of geology and geography-2019, Khurel Togoot. p. 149-153.

- Ninomiya, Y. 2002. Mapping quartz, carbonate minerals, and mafic ultramafic rocks using remotely sensed multispectral thermal infrared ASTER data: Proceedings of SPIE - The International Society for Optical Engineering. p. 191-202.  
<https://doi.org/10.1117/12.459566>
- Ourhzif, Z., Algouti, A., Algouti, A., Hadach, F. 2019. Lithological mapping using Landsat 8 oli and ASTER multispectral data in Imini-Ounilla District south High Atlas of Marrakech: The international archives of the Photogrammetry, Remote sensing and Spatial Information Sciences. XLII-2/W13, p. 1255-1262. <https://doi.org/10.5194/isprs-archives-XLII-2-W13-1255-2019>
- Platt, J. 1998. Sequential Minimal Optimization: A Fast Algorithm for Training Support Vector Machines. Advances in Kernel Methods-Support Vector Learning. 208.
- Rezaei, A., Hassani, H., Moarefvand, P., Golmohammadi, A. 2019. Lithological mapping in Sangan region in Northeast Iran using ASTER satellite data and image processing methods: Geology, Ecology, and Landscapes, v. 4(1), p. 59-70.  
<https://doi.org/10.1080/24749508.2019.1585657>
- Rowan, L.C., Mars, J.C. 2003. Lithologic mapping in the Mountain Pass, California area using advanced spaceborne thermal emission and reflection radiometer (ASTER) data: Remote Sensing of Environment, v. 84 (3), p. 350-366.  
[https://doi.org/10.1016/S0034-4257\(02\)00127-X](https://doi.org/10.1016/S0034-4257(02)00127-X)
- Sabins, F. 1987. Remote sensing: Principles and interpretation (2nd ed.). New York, NY: Freeman.
- Son, Y.S., Kang, M., Yoon, W. 2012. Regional mapping of alteration of the Oyu Tolgoi Cu-Au deposit in Mongolia using band math method with ASTER image: Korean Society for Geosystem Engineering. v. 49. p. 157-165. (in Korean with English abstract)
- Son, Y.S., Kim, K.E., Yoon, W.J., Cho, S.J. 2019. Regional mineral mapping of island arc terranes in southeastern Mongolia using multi-spectral remote sensing data: Ore Geology Reviews. v. 113. 103106.  
<https://doi.org/10.1016/j.oregeorev.2019.103106>
- Son, Y.S., You, B.W., Bang, E.S., Cho, S.J., Kim, K.E., Baik, H., Nam, H.T. 2021. Mapping Alteration Mineralogy in Eastern Tsogtsetsii, Mongolia, Based on the WorldView-3 and Field Shortwave-Infrared Spectroscopy Analyses: Remote Sensing. v. 13, p. 914.  
<https://doi.org/10.3390/rs13050914>
- Stoltz, T.A. 2008. Geological Mapping of Orhon, Tariat, and Egiin Dawa, Central Mongolia, through the Interpretation of Remote Sensing Data: Master's thesis, Wright State University, Ohio.
- Tomurtogoo, O. 2017. Tectonic subdivision of Mongolia at the scale of 1:3 000 000. Mineral Resource Authority of Mongolia.
- Watts, D., Harris, N. 2005. Mapping granite and gneiss in domes along the North Himalaya antiform with ASTER SWIR band ratios: Geological Society of America Bulletin. v. 117(7-8), p. 879-886.  
<https://doi.org/10.1130/B25592.1>
- Zhang, X., Li, P. 2014. Lithological mapping from hyperspectral data by improved use of spectral angle mapper: International Journal of Applied Earth Observation and Geo-information, v. 31, p. 95-109.  
<https://doi.org/10.1016/j.jag.2014.03.007>